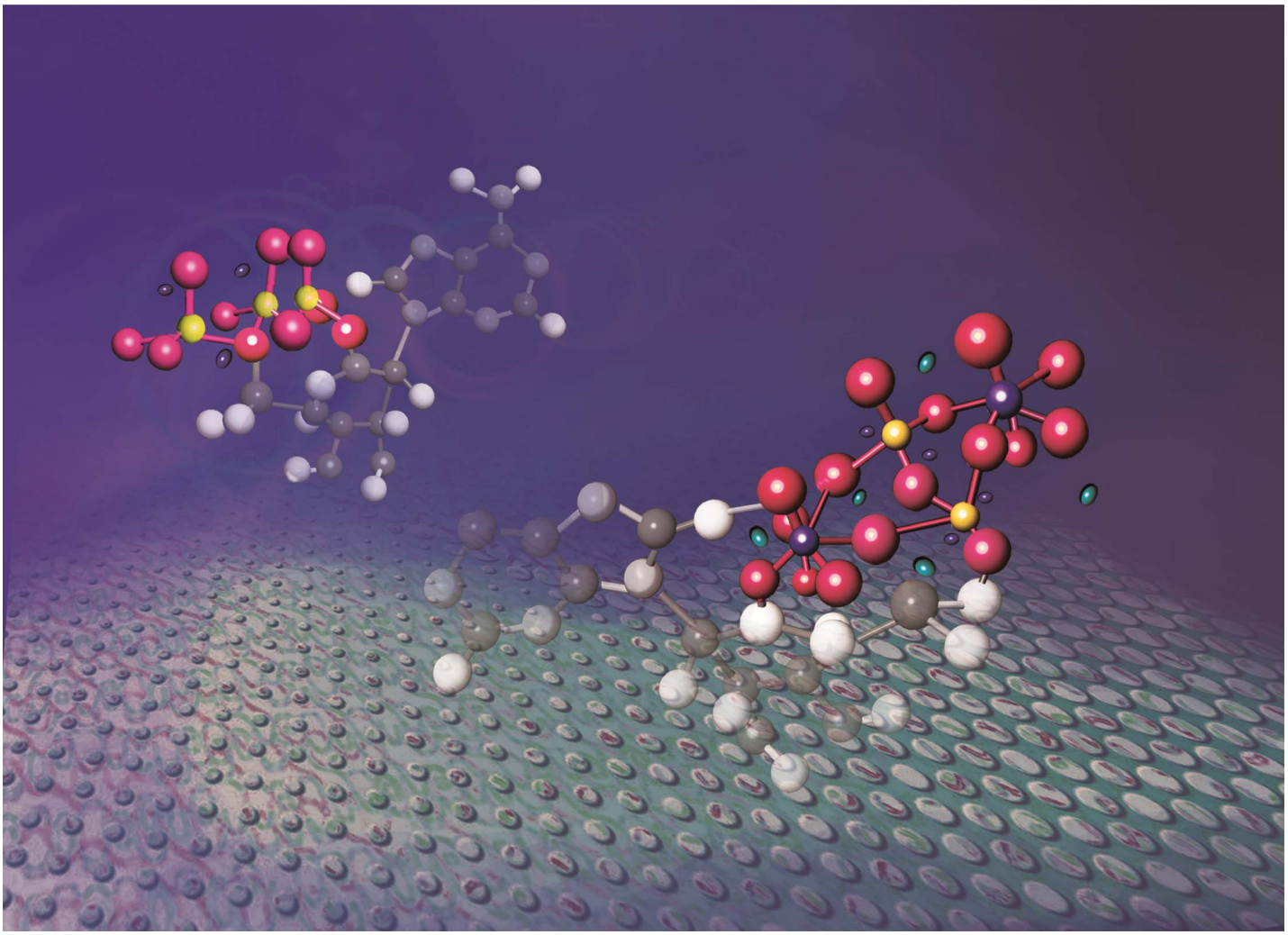

Joint research work from School of Materials Science and Engineering, Qilu University of Technology, Section of Chemistry, Aalborg University, International Center for Dielectric Research, Xian Jiaotong University and State Key Laboratory of Crystal Materials, Shandong University.

Title: Fabricating high-energy quantum dots in ultra-thin $LiFePO_4$ nanosheets using a multifunctional high-energy biomolecule—ATP

We report an important advance in the development of a new type of nanostructure of $LiFePO_4$ and particular electrochemical properties by a green biological method.

As featured in:

See Xudong Zhang, Wen He, Yuanzheng Yue *et al.*, *Energy Environ. Sci.*, 2014, **7**, 2285.

ROYAL SOCIETY OF CHEMISTRY

www.rsc.org/ees

Registered charity number: 207890

Energy & Environmental Science

PAPER

View Article Online
View Journal | View Issue

Cite this: *Energy Environ. Sci.*, 2014, 7, 2285

Fabricating high-energy quantum dots in ultra-thin $LiFePO_4$ nanosheets using a multifunctional high-energy biomolecule—ATP†

Xudong Zhang,*[a] Zhiying Bi,[a] Wen He,*[a] Guang Yang,[c] Hong Liu[d] and Yuanzheng Yue*[ab]

Received 28th December 2013
Accepted 11th March 2014

DOI: 10.1039/c3ee44187c

www.rsc.org/ees

By using a multifunctional high-energy biomolecule—adenosine triphosphate (ATP)—we fabricated high-energy quantum dots (HEQDs) with a feature size of less than 10 nm and used them in high-power lithium-ion batteries. We introduced high-energy phosphate bonds into the crystal structure of $LiFePO_4$ nanoparticles and synthesized the mesoporous biocarbon nanowire coated $LiFePO_4$ with HEQDs (MBCNW-LFP-HEQDs) by using ATP as a phosphorus source, a nucleating agent, a structural template and a biocarbon source. HEGDs were homogeneously formed inside the ultra-thin $LiFePO_4$ nanosheet and the mesoporous biocarbon nanowire network structure was coated on the surface of the nanosheet. In $LiFePO_4$ nanoparticles, HEQDs result in more storage sites of Li^+ ions and easier transfer kinetics of electrons and lithium ions, where the kinetic transformation path between $LiFePO_4$ and $FePO_4$ is rather different from the path deduced from its equilibrium phase diagram. Compared to the usual $LiFePO_4$ nanoparticle (10–100 nm) cathode, the MBCNW-LFP-HEQD cathode shows the best first discharge capacity of 197 mA h g^{-1} at the 0.1 C rate, which is higher than the theoretical capacity of $LiFePO_4$ (170 mA h g^{-1}). After 100 cycles at varied current rates: 0.1, 0.5, 1, 5 and 10 C, this cathode still delivered a high discharge capacity of 180 mA h g^{-1} and an ultra-high coulombic efficiency close to 100%. This is attributed to the quantum tunneling of HEQDs in $LiFePO_4$ nanoparticles and better percolation of mesoporous biocarbon nanowire coating network structures. This work is instructive for fabrication and design of new types of electrochemical energy conversion and storage devices with extraordinary properties and functions.

Broader context

Nanostructure lithiated iron phosphate ($LiFePO_4$) has been considered as the most promising cathode candidate because of its inherent merits including low toxicity, potential for low cost, long cycle ability and high safety. Currently, one of the most popular topics is the development of controllable fabrication technology of nanosized particles. In this contribution, we report on a new technique for fabricating sub-10 nm high-energy quantum dots (HEQDs) in ultra-thin $LiFePO_4$ nanosheets and synthesizing the mesoporous biocarbon nanowire coating $LiFePO_4$ nanosheets with HEQDs using a high-energy biomolecule—ATP. This nanostructure provides more storage sites of Li^+ ions and easier transfer kinetics of electrons and lithium ions, and displays the superior discharge capacity and an ultra-high coulombic efficiency. The fabrication strategy presented here is facile, cost-effective, and scalable, and opens up new avenues for developing optimal nanocomposite cathode materials for high performance lithium-ion batteries.

1. Introduction

The electrode materials for the next-generation of large-scale lithium-ion batteries used for hybrid electric vehicles (HEVs) or electric vehicles (EVs) should not only fulfill the safety standard, but also possess good rate performance for both charge and discharge of batteries.[1–3] In this context, nanostructured lithiated iron phosphate ($LiFePO_4$) has been considered as the most promising cathode candidate because of its inherent merits including low toxicity, low cost, long cycle ability and high safety.[4–6] However, as $LiFePO_4$ nanoparticles have higher surface area and lower crystallinity compared to conventional $LiFePO_4$ materials, more electrolyte is decomposed on the nanoparticle surface, leading to the enhanced formation of solid–electrolyte interfaces. This also lowers coulombic efficiency, which is one of the critical parameters for practical utilization of electrode materials, resulting in fewer storage sites of Li^+ ions and sluggish kinetics of electrons and lithium

[a]*Institute of Materials Science and Engineering, Qilu University of Technology, Jinan 250353, China. E-mail: zxd1080@126.com; hewen1960@126.com; Fax: +86 531 89631080; Tel: +86 531 89631518*

[b]*Section of Chemistry, Aalborg University, DK-9000 Aalborg, Denmark. E-mail: yy@bio.aau.dk*

[c]*International Center for Dielectric Research, Xian Jiaotong University, Xian, 710049, China*

[d]*State Key Laboratory of Crystal Materials, Shandong University, Jinan 250100, China*

† Electronic supplementary information (ESI) available. See DOI: 10.1039/c3ee44187c

ions.[7,8] Recently, scientists have made progress in removing Li transport limitations in $LiFePO_4$ through a combination of the following factors: reducing the active particle size to the nanoscale, coating active particles with carbon, incorporating dopant impurities, diluting the active mass within the electrode with the electrochemically inactive material, and coating active particles with glassy ionic conductors. Despite this progress, the innate rate capability of $LiFePO_4$ is revealed to be still higher.[9] Unfortunately, it is very difficult to achieve the theoretical capacity (170 mA h g^{-1}) of $LiFePO_4$ because of its intrinsic slow diffusion for Li^+ and very low electronic conductivity. The specific capacity of commercially available cathode carbon-coated nanosized $LiFePO_4$ (10–100 nm) is typically 120–160 mA h g^{-1}. Therefore, the controllable fabrication of nanosized particles is a key for enhancing the electron transfer and lithium ion diffusion.[10]

Defect-free crystalline $LiFePO_4$ has an olivine structure (*Pnma*) and a $Fe^{2+/3+}$ redox couple at 3.5 V. $LiFePO_4$ stores Li through a two-phase transformation between $FePO_4$ and $LiFePO_4$ in equilibrium states. Li-ion diffusion in the lattice is uniaxial along the *b*-direction [010] channel *via* a nonlinear, curved trajectory between Li sites.[11–14] G. Ceder *et al.*[15] have demonstrated why $LiFePO_4$ functions as a cathode at a reasonable rate. The reason is attributed to the existence of a single-phase transformation path at a very low overpotential, allowing the system to bypass nucleation and growth of a second phase. The single-phase metastable transformation path is facile in non-equilibrium states. Since lithiation in the nanoparticles occurs more homogeneously than that in the two-phase model, the stresses in the system are reduced, and thus the cycling behaviour of $LiFePO_4$ electrodes is improved. Despite the progress, researchers still continue to seek even better electrochemical systems with new phase transformation mechanisms for the next-generation lithium-ion batteries.

Quantum dots (QDs) (<10 nm) are quasi zero dimension nanodomains containing only a small number of atoms. Owing to an extremely high surface-to-mass ratio of QDs, much more atoms are situated on the surface compared to bulk materials. The surface atoms possess higher energy of delocalized electrons and hence are kinetically more active than the interior atoms. As a consequence, QDs will have more sites bearing more lithium ions. QDs have become the center of an ever growing research effort because of their size effects, significantly enhanced kinetics, fascinating physical properties such as quantum electronic transport, quantum confinement effect, quantum tunneling effect, extremely high electron mobility, and interesting for both fundamental science and applications.[16] Beyond the 10 nm technology, the quantum nature of atoms and molecules is expected to increase the transport of Li^+ ions and electrons in electrodes and to harvest the extremely useful electrochemical performances as additional charge carriers *via* hole traps.[17] HEQDs in $LiFePO_4$ nanoparticles imply that the theoretical capacity (170 mA h g^{-1}) of crystalline bulk $LiFePO_4$ can be surpassed by that of QDs.[18] In contrast to crystalline $LiFePO_4$, little is known about the Li transport in QDs, but this leaves more space for further deep understanding.

In nanotechnology applications, great attention has been paid to biomaterial systems to discover new self-assembly techniques. The interaction of nanoparticles with proteins, peptides, and DNA has been studied for innovative and robust nanomaterial designs.[19,20] Nanobiotechnology is one of the most powerful routes for organizing a nanoscale system with the highest accuracy. Biological systems can produce extraordinary inorganic structures and morphologies.[21–24] In this work, we develop a new technique for fabricating high-energy quantum dots (HEQDs) in ultra-thin $LiFePO_4$ nanosheets and synthesizing the mesoporous biocarbon nanowire coating $LiFePO_4$ with HEQDs (MBCNW-LFP-HEQDs) using a high-energy biomolecule—ATP as a phosphorus source, a nucleating agent, a structural template and a biocarbon source. We demonstrate the quantum confinement effect and tuning of the electrochemical performances for breaking through theoretical capacity of $LiFePO_4$. Electrons and Li ions can be easily transported to the HEQDs due to its tunneling barrier, which is lower than that of the usual $LiFePO_4$ nanoparticles (10–100 nm) (ULFPNP, the ULFPNP sample is from Peking University leading Science and Technology Industry Co., Ltd.). This new technique has two important advantages: the Li transport rate in HEQDs is higher than that in ULFPNPs due to the structural disorder; and the electrode capacity of HEQDs is larger than the theoretical capacity of bulk crystalline $LiFePO_4$. Besides the obvious huge increase in capability value and coulombic efficiency of $LiFePO_4$, they can be synthesized more easily and with low cost; they can self-assemble and, most importantly, they can display new electrochemical performances and behaviors. Such a simple and scalable approach may also be applied to other cathode systems, boosting up the capacity for various Li batteries.

2. Experimental

Synthesis of MBCNW-LFP-HEQDs

The reagents used in this work include $FeCl_3$ (99%, Tianjin Kermel Chemical Reagent Co., Ltd.), acyl nucleoside triphosphate disodium salt (Na_2ATP, 10 mg ml^{-1}, Xuzhou Ryen Pharma. Co., Ltd.), HCl (36–38%, Laiyang Economic and Technological Development Zone Fine Chemical Plant), ascorbic acid (99.5%, Tianjin Bodi Chemical Co., Ltd.), and Li_2CO_3 (97%, Tianjin Damao Chemical Co., Ltd.). Distilled water was used during synthesis of the samples.

MBCNW-LFP-HEQDs were prepared using the biotemplate and carbon thermal reduction method. The general synthesis procedure is described as follows. Na_2ATP in a stoichiometric ratio was added into a beaker and incubated for 30 min at different temperatures (30, 40 and 50 °C) in a water bath pot. Then the Na_2ATP was immediately cooled with liquid nitrogen to release the surface charge of anionic phosphate groups in the ATP biomolecule, and thus the Na_2ATP biotemplate solution were obtained. $FeCl_3$ was dissolved in distilled water and added to the Na_2ATP biotemplate solution with magnetic stirring at room temperature, and then adjusted pH to 3 with HCl. A yellow solution with the $FePO_4$ sediment was formed. Finally, the mixture solutions were stirred vigorously for 12 hours. The $FePO_4$ sediment was dried in an oven at 120 °C for constant weight, and

then the dried $FePO_4$ mixture was washed and centrifuged two times with distilled water to remove the soluble sodium ions, and then dried to a constant weight in an oven at 120 °C again. The dry $FePO_4$–ATP mixtures were mixed with Li_2CO_3 and ascorbic acid in the stoichiometric ratio—$n_{Fe} : n_{Li} : n_{acid} = 1 : 1 : 1$ for 6 h through a dry ball-milling process. The resulting mixtures were annealed at 300 °C for 3 h, and then sintered at different temperatures (700, 750 and 800 °C) in a N_2 atmosphere for 8 h. The heating rate was kept relatively low, *i.e.*, 5 °C min^{-1}, to avoid structural collapse due to fast crystallization. The final product obtained was in the form of black powder, and the samples were marked as MBCNW-LFP-HEQD-1 (with the ATP biotemplate incubated at 30 °C), MBCNW-LFP-HEQD-2 (with the ATP biotemplate incubated at 40 °C), MBCNW-LFP-HEQD-3 (with the ATP biotemplate incubated at 50 °C).

Characterization

The morphology, porous structure and crystal structure of the synthesized samples were characterized using a high-resolution transmission electron microscope (HRTEM) and an atomic force microscope (AFM). HRTEM images were obtained using a Philips Tecnai 20U-TWIN microscope, working at 300 kV. A trace amount of sample was dispersed in ethanol solution by sonication, and then deposited on a carbon-coated copper grid. HRTEM images were obtained at the Scherzer defocus ($\Delta f = -41.25$ nm) to optimize the transfer function of the optical system balancing the effect of spherical aberration. AFM measurements were carried out using an atomic force microscope (IIIa AFM), and the samples were prepared by adding the ethanol suspension with the dispersed particles dropwise onto a freshly cleaved mica piece. Energy-dispersive spectrometer (EDS) measurements were performed using a JEM-ARM200F scanning transmission electron microscope (STEM). X-ray photoelectron spectroscopy (XPS) measurements were performed using a Kratos Axis Ultra DLD (delay line detector) spectrometer equipped with a monochromatic Al Kα X-ray source (1486.6 eV). The phase composition of the synthesized samples were analyzed by X-ray diffraction (XRD) employing a Cu-Kα X-ray diffractometer (PANalytical X'Pert PRO; Netherlands). The diffraction patterns were collected over a diffraction angle 2θ range of 5–90°, with an acquisition time of 12 s at 0.02° step size. The N_2 adsorption–desorption isotherms and Barrett–Joyner–Halenda pore size distributions were carried out at 77 K using a automatic surface area analyzer (Micromeritics, Gemini V2380, USA) under continuous adsorption conditions. Fourier transform infrared spectroscopy (FT-IR) measurements were performed using a Nicolet Nexus spectrometer (Nicolet, NEXUS 470, USA) and by using a KBr wafer technique. The carbon content in the samples was determined using a Vario EL IIICHN elemental analyzer. The fluorescence of the sample was probed directly using a ECLIPSE80i Fluorescent microscope (Nikon, Japan).

Electrochemical evaluation

The charge–discharge performances were determined with CR 2032 coin cells. The cathode materials were prepared by mixing the synthesized sample with acetylene black and polyvinylidene fluoride (PVDF) in a weight ratio of 85 : 5 : 10 in *N*-methyl pyrrolidone to ensure homogeneity. Then the mixture was pressed to a piece on an Al-foil with about 0.02 mm in thickness, dried under an air atmosphere at 60 °C for 5 h and a vacuum atmosphere at 120 °C for 8 h and cut into circular strips of 15 mm in diameter. The mass calculation of active materials was carried out based on the 85% of difference between the mass of synthesized materials coated Al foil and the mass of pristine Al foil. The cells were assembled in a glove box filled with high-purity argon, where lithium metal was used as an anode, a polypropylene film as the separator, and 1 M $LiPF_6$ in an electrolyte consisting of ethylene carbonate–dimethyl carbonate–ethylene methyl carbonate in a volume ratio of 1 : 1 : 1. The charge–discharge performances of the synthesized samples were tested using a Channels battery analyzer (CT3008W) at different current densities between 2.5 and 4.2 V cut-off voltages using the coin-cells. The electrochemical impedance (EIS) and cyclic voltammetry (CV) measurements were performed with a PARSTAT 2263 electrochemical workstation. EIS was also recorded with the frequency ranging from 100 kHz to 10 mHz and a AC signal of 5 mV in amplitude as the perturbation. The voltage range of the CV measurements was 2.5–4.2 V and the scanning rate was from 0.1 to 1 mV s^{-1}. All the tests were performed at room temperature.

3. Results and discussion

ATP-enhanced electrochemical performances of the nanostructured $LiFePO_4$ were first demonstrated. A schematic diagram of a biological method is summarized in Fig. 1. Adenosine triphosphate (ATP) is the high-energy biomolecule and its critical part is the phosphorus part—the triphosphate. There are high-energy phosphorus bonds in the triphosphate and they release a large amount of free energy upon the reaction,[25,26] which can be used as a phosphorus source and a nucleating agent during the synthesis. The structure of ATP has an ordered carbon compound backbone, which can be used as a structural template and a biocarbon source. Three phosphorus groups are connected by oxygen ions, and each of these oxygens has a negative charge, causing repulsion force among these oxygens, *i.e.*, increasing the potential energy (Fig. 1a). So the ATP exhibits increased interactions with Fe cations and can serve as a nucleating agent for active iron phosphate growth. During incubation with the iron chloride precursor, all ATP biomolecules were loaded with iron ions to synthesize active $FePO_4$ and a complex structure was formed by the self-assembly of iron ions and ATP biomolecules (Fig. 1b). During pyrolytic degradation, the carbon compound backbone of ATP is decomposed to form a mesoporous biocarbon nanowire network, while an external or internal self-created atmosphere can prevent Fe^{2+} from oxidation and effectively restricts the growth of the $LiFePO_4$ nanoparticles (Fig. 1c). The high-energy phosphorus bonds form HEQDs in $LiFePO_4$ nanoparticles. In the synthetic process, the chemical bond linkages between ATP biomolecules with iron ions and the *in situ* nanocomposite linkages between $LiFePO_4$ nanosheets with the mesoporous biocarbon nanowire network were studied by FT-IR (see

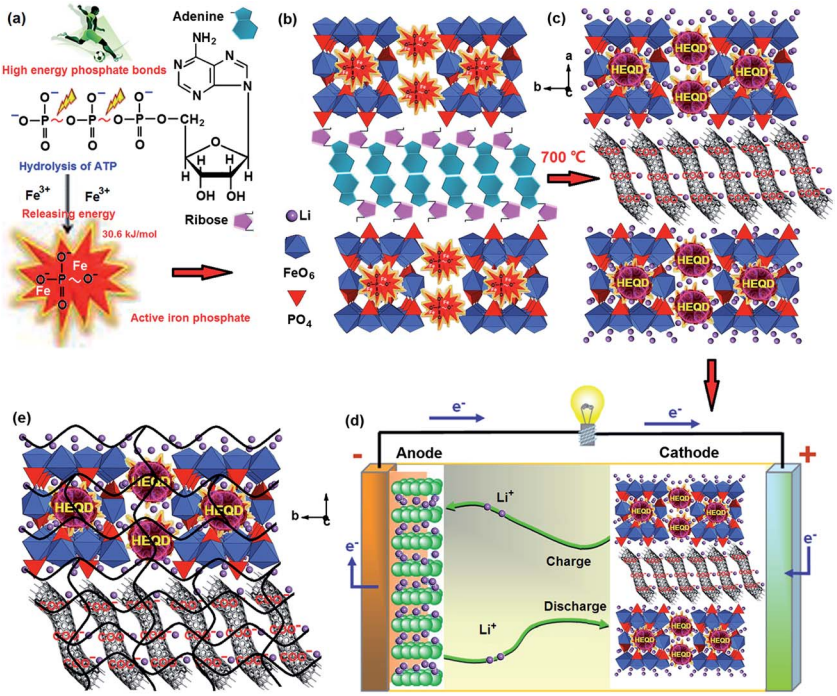

Fig. 1 A biological method: self-assembly and multiple functions of ATP high-energy biomolecules. (a) A schematic presentation of the multifunctional ATP biomolecule. (b) A schematic diagram of self-assembly of the multifunctional ATP biomolecules with iron phosphate. (c) Structure model of MBCNW-LFP-HEQDs. (d) A schematic drawing of the battery used MBCNW-LFP-HEQDs as cathodes. (e) Schematic illustration of Li^+ diffusion in the two-dimensional channel of MBCNW-LFP-HEQDs. Black curves represent the two dimension diffusion pathways for Li ions in the lattice.

Fig. S2d†). The results indicate that hydroxyl (OH^-) in the ribose and OPO_3^{2-} radicals in the triphosphate part play the important role in the chemical interaction between the ATP biomolecules and the iron ions. The decrease of the P–O bond length shows that the high-energy phosphate bonds have been introduced into the crystal structure of $LiFePO_4$ nanoparticles (Table S2j†). There are *in situ* nanocomposite linkages between the $LiFePO_4$ nanoparticles and the mesoporous biocarbon nanowire coating network. The X-ray diffraction patterns of the synthesized samples (Fig. S2a and b†) show only the peaks indexed as $LiFePO_4$. Through the XRD and FT-IR spectroscopy results, we have verified that the deposition and self-assembly mechanism shown in Fig. 1 is feasible for synthesizing MBCNW-LFP-HEQDs.

The synthesized material was assembled as a cathode in a lithium-ion battery using lithium metal foil as a negative electrode (Fig. 1d). The results obtained by battery tests show that the sample has good reversibility, excellent discharge capacity and ultra-high coulombic efficiency. The total channel length between surfaces of HEQDs is very small (<5 nm) (Fig. 2a), and all sites are available by rapid diffusion through unblocked channels. Li^+ ions can circumvent HEQDs by migrating between different channels. The HEQDs offer such an opportunity for Li^+ to cross channels (Fig. 1e).

HRTEM is a powerful tool to study properties of materials on the atomic scale that allows for direct imaging of the atomic structure of the sample. HRTEM image formation relies on phase contrast. The phase contrast imaging technique is very sensitive to the sample thickness. The interaction of the electron wave with the crystallographic structure of the sample is complex and in this case the image cannot be interpreted in terms of crystal structure projection, but a qualitative idea of the interaction can readily be obtained.[27] In order to probe the fine nanostructure of $LiFePO_4$, HRTEM analysis was employed and the images were recorded at a negative Scherzer defocus. Fig. 2a and b show HRTEM images of a $LiFePO_4$ nanosheet with HEQDs and a normal crystalline $LiFePO_4$ nanoparticle without HEQDs (ULFPNP), respectively. According to the image contrast mechanism in the Weak Phase Object (WPO) approximation,[28] the ultra-thin $LiFePO_4$ nanosheet shown in Fig. 2a and the ultra-thin edge of the ULFPNP shown in Fig. 2b can be identified as the WPO, and at the negative Scherzer defocus Li atomic columns in the β Li-rich phase ($Li_\beta FePO_4$) are imaged as bright spots. It is found that Fig. 2a shows a brighter background than that shown in Fig. 2b, implying that the particle shown in Fig. 2a is thinner. Fig. 2a shows that the HEQDs with an average size of about 3 nm (see the dark spots enclosed by the red rings) are embedded in an ultra-thin $LiFePO_4$ nanosheet, and that there are distinct lattice dislocations and various antisite defects in the HEQD nanocrystal domains. The HEQDs appear as dark spots because the HEQD has a higher atomic density. The existence of HEQDs in the $LiFePO_4$ structure was also confirmed by the AFM image (Fig. 2c) and the fluorescent micrograph (Fig. 2e) of the MBCNW-LFP-HEQD-2 sample. Fig. 2c shows the size and height distributions of HEQDs embedded in a ultra-thin $LiFePO_4$ nanosheet, where the

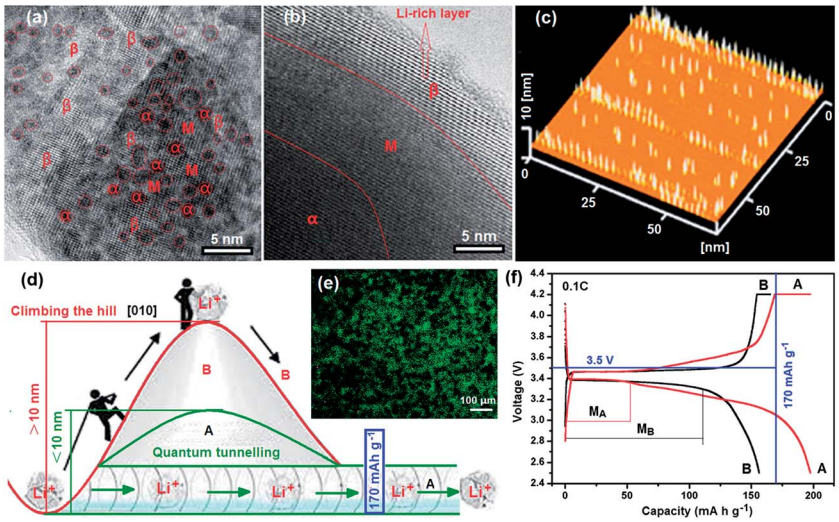

Fig. 2 Characterizations of HEQDs. (a) HRTEM image of HEQDs (area containing the red ring) embedded in a ultra-thin $LiFePO_4$ nanosheet in the MBCNW-LFP-HEQD-2 sample. (b) HRTEM image of a ULFPNP, only showing lattice fringes, $Li_\alpha FePO_4$ (α-Li-poor phases), $Li_\beta FePO_4$ (β-Li-rich phases) and binary phase distribution (M – metastable miscibility gap). (c) AFM image shows the size and height distributions of HEQDs embedded in a ultra-thin $LiFePO_4$ nanosheet. (d) Li ion pathway diagrams in ULFPNP (B) and MBCNW-LFP-HEQDs (A). (e) Fluorescent micrograph of the MBCNW-LFP-HEQD-2 sample, which exhibits green fluorescence at the excitation wavelengths of 480 nm. (f) The first discharge and charge profiles of the MBCNW-LFP-HEQD-2 cathode (A) and the ULFPNP cathode (B) at 0.1 C rate using CR 2032 coin cells. The carbon content for the MBCNW-LFP-HEQD-2 sample is 12.85 wt%.

standing yellow rods represent HEQDs with a height of 10 nm. Fig. 2e exhibits green fluorescence at the excitation wavelength of 480 nm. However, there is no dark spot shown in Fig. 2b, only showing regular lattice fringes of $LiFePO_4$. The area between the darker α Li-poor phase ($Li_\alpha FePO_4$) and the brighter β Li-rich phase ($Li_\beta FePO_4$) is a miscibility gap marked as M.[29] The mobility limitation of the two-phase boundary of $FePO_4$–$LiFePO_4$ formed owing to lithium extraction from $LiFePO_4$ could be diminished in a solid solution, Li_xFePO_4.[30] However, the M of the $Li_\alpha FePO_4$–$Li_\beta FePO_4$ binary phase has almost vanished as shown in Fig. 2a.[31] We found that the average number, size and distribution of HEQDs in the $LiFePO_4$ nanosheet can be controlled by changing the incubating temperature of ATP and the growth time during the synthesized process (ESI Fig. S1†), thus providing a way of controlling the growth of HEQDs for different applications.

Ceder *et al.*[32] demonstrated that most channels in small enough nanoparticles are unblocked, making all sites accessible by very rapid migration of Li^+ through the channels. The QDs can not only store quickly more Li ions because of the higher specific surface area, but also increase the Li^+ conductivity and the electrochemical reaction centers, and also reduce the effective diffusion length of Li^+ ions because of the small size of channels. Especially, since the interfaces among QDs account for several tens of percentage by volume, the interfacial effect is dominant in overall lithium transport. The interfaces of QDs act as fast pathways for Li^+ ions and provide more active sites for Li^+ ions in $LiFePO_4$, and hence, enhance the lithium ion intercalation and deintercalation, leading to an extra storage of Li^+ and a high capacity.[33,34] Therefore the excessive lithium storage could explain why the theoretical capacity value of $LiFePO_4$ is surpassed. QDs alter the $LiFePO_4$ phase transition pathways during the electrochemical process. To demonstrate this effect, the first discharge and charge profiles of the MBCNW-LFP-HEQD-2 cathode (A) and the ULFPNP cathode (B) at the 0.1 C rate using CR 2032 coin cells are compared and analyzed (Fig. 2f, AB). Unfortunately, in the ULFPNP structure, even the lowest energy path, which occurs by Li migrating to the nearest Li channel through a vacant intermediate Fe^{2+} site, has an activation barrier much higher than that within a certain channel (Fig. 2d, B). So it is very difficult to achieve the theoretical capacity of $LiFePO_4$ because of fewer storage sites of Li^+ ions and sluggish kinetics of electrons and lithium ions in the ULFPNP structure (Fig. 2f, B). Based on the understanding of anti-site defects, the HEQD is a promising way to contribute to high electronic conductivity. Two-dimensional diffusion in the $LiFePO_4$ nanosheet with HEQDs is significantly different from one-dimensional diffusion in ULFPNPs. The presence of HEQDs has a drastic effect on the rate, at which Li ions can move through the $LiFePO_4$ crystal *via* quantum tunnelling (Fig. 2d, A) and can make Li channels cross-over possible (Fig. 1e). Therefore, the first discharge capacity of the MBCNW-LFP-HEQD-2 cathode can break through the theoretical capacity of $LiFePO_4$ and delivered the best high first discharge capacity of 197 mA h g^{-1} (116% of the theoretical value) at the 0.1 C rate (Fig. 2f, A). Comparing with the miscibility gap M_B of the ULFPNP cathode (Fig. 2f, B), HEQDs in a single $LiFePO_4$ nanosheet are in an instability state due to increased interface energy, resulting in a decrease of the miscibility gap M_A (Fig. 2f, A) of the MBCNW-LFP-HEQD cathode and a increase of the solid solution region of $LiFePO_4$.[35] Compared with other material design as we published previously,[21,22] although the electrochemical properties of synthesized cathodes were enhanced and the cathode delivered the best high first discharge capacity

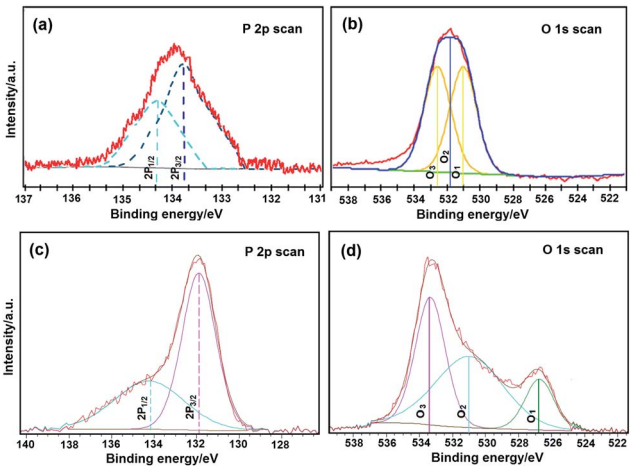

Fig. 3 High-resolution X-ray photoelectron spectra (HRXPS). (a) Phosphorus 2p (P 2p) HRXPS from the ULFPNP sample. (b) Oxygen 1s (O 1s) HRXPS from the ULFPNP sample. (c) P 2p HRXPS from the MBCNW-LFP-HEQD-2 sample. (d) O 1s HRXPS from the MBCNW-LFP-HEQD-2 sample. The jagged lines represent the unsmoothed raw data, and the solid lines represent the sum of each curve fitted component.

of 160.4 mA h g^{-1} at the 0.1 C rate, it also is very difficult to achieve the theoretical capacity of $LiFePO_4$. Based on the above analysis, it is clear that Li ions in the MBCNW-LFP-HEQD cathode can migrate more quickly along the Li-ion channels, and this may improve the ionic properties of $LiFePO_4$.

To investigate the role of high-energy phosphate bonds in the crystal structure of $LiFePO_4$ nanoparticles, high-resolution X-ray photoelectron spectroscopy (HRXPS) was applied. Fig. 3 shows phosphorus 2p (P 2p) and oxygen 1s (O 1s) HRXPS curves from the ULFPNP and MBCNW-LFP-HEQD-2 samples, respectively. In P 2p HRXPS, the spectra were fitted to the P 2p doublet, the $2p_{1/2}$ peak and the $2p_{3/2}$ peak, which is split by 0.5 eV. The higher energy, the lower intensity peak is the $2p_{1/2}$ peak, and another is the $2p_{3/2}$ peak. They show two different chemical states for phosphorus. In O 1s HRXPS, the spectra were fitted to the O 1s three peaks, O_1, O_2 and O_3. They show three different chemical states for oxygen. The O_1 species at the low binding energy belong to $O_2^{\bullet}$ ions, whereas O_2 species with a medium binding energy are attributed to $O^{\bullet}$ and $O_2^{\bullet}$ ions in the oxygen deficient regions mainly caused by oxygen vacancies, V_O. The high binding energy species O_3 belong to the absorbed or dissociated oxygen or OH species on the surface of the sample.[36] The fitted comparison data of P 2p and O 1s peaks for ULFPNP and MBCNW-LFP-HEQD-2 samples are presented in Table S1.† In Table S1,† it is found that the binding energy at the $2p_{3/2}$ peak and the O_1 1s peak from MBCNW-LFP-HEQD-2 is much lower than those of ULFPNPs and the feature of their O 1s HRXPS is different, revealing that there are high-energy phosphate bonds in the crystal structure of MBCNW-LFP-HEQD-2. Besides, the percentage of O_2 species in ULFPNP and MBCNW-LFP-HEQD-2 samples were 15.2% and 22.6%, respectively. Therefore, the MBCNW-LFP-HEQD-2 sample has more oxygen vacancies and higher activity, which are associated with active sites for high-energy phosphate bonds and could contribute to higher rate performance. This is consistent with the HRTEM results (see Fig. 4f).

To understand the effect of ATP biotemplates on the structure of synthesis materials, we characterized the synthesized samples using various methods. Fig. 4 shows HRTEM images of

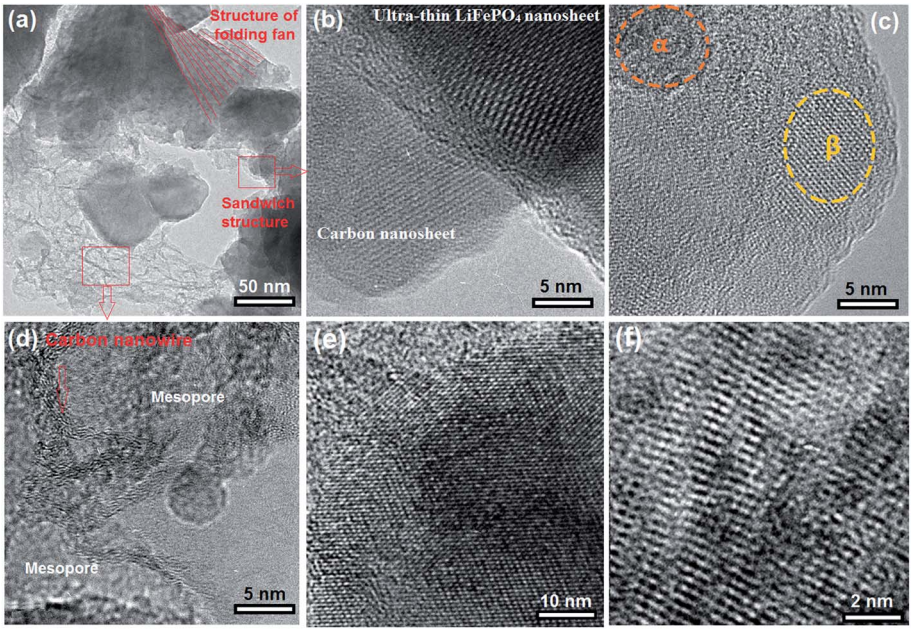

Fig. 4 HRTEM images of the MBCNW-LFP-HEQD-2 sample. (a) A low magnification image, showing structures of folding fan and sandwich. (b) An enlarged image, showing the nanosheet heterostructures of ultra-thin $LiFePO_4$ and biocarbon. (c) An enlarged image, showing HEQDs with α-Li-poor phases and β-Li-rich phases in an $LiFePO_4$ nanosheet. (d) An enlarged image, showing the mesoporous biocarbon nanowire network structure. (e) Lattice image of a $LiFePO_4$ nanosheet. (f) An enlarged image in (e), showing the various anti-site lattice defects.

the MBCNW-LFP-HEQD-2 sample. In Fig. 4a it is seen that the MBCNW-LFP-HEQD-2 sample has the layer structures with folding fan and sandwich. $LiFePO_4$ nanosheets were tethered to biocarbon nanosheets mainly through the mesoporous biocarbon nanowire attachment. This indicates the precipitation reactions of $LiFePO_4$ nanoparticles occur on the ATP biomolecules. The brightest area shown in Fig. 4a corresponds to monolayers, whereas the darker area is composed of more layers of nanosheets. Fig. 4b shows an ultra-thin $LiFePO_4$ nanosheet and a biocarbon nanosheet. Fig. 4c exhibits the HEQDs with the α-Li-deficient phase ($Li_\alpha FePO_4$) and the β-Li-rich phase ($Li_\beta FePO_4$) in an ultra-thin $LiFePO_4$ nanosheet. Fig. 4d shows the biocarbon nanowire structures. The highly conductive mesoporous biocarbon nanowire wrapping around the $LiFePO_4$ nanosheet assists the electron migration during the charge/discharge processes, diminishing the irreversible capacity at the first cycle and leading to higher coulombic efficiency without fading at various C-rates. Effective electron transport is another important requirement for kinetics, since insertion/extraction of Li ions must be accompanied by electrons transfer to keep the charge balance. Fig. 4e shows a lattice image of the ultra-thin $LiFePO_4$ nanosheet, exhibiting the partial densities of states of Fe, P, O and Li atoms in the $LiFePO_4$ nanosheet structure with the stoichiometry and Li/Fe exchange-defects. In other words, it can be clearly seen that $LiFePO_4$ with the Li/Fe exchange defect has more electron states, which is another favorable condition to achieve higher electronic conductivity.

Anyway, the special electronic structure ensures that the material with the Li/Fe exchange defect may exhibit a higher discharge capacity (Fig. 2f, A). Controlling the concentration, type and segregation of the native defects *via* tuning the synthesis conditions is an instructional way to enhance the electrical conductivity of $LiFePO_4$. It should be mentioned that anti-site defects sometimes offer an opportunity for Li ions to cross-over between channels. The antisite defect in the $LiFePO_4$ structure is a kind of intrinsic defect, which is easily formed during the synthesis process. They are characterized by an exchange of Li and Fe in the lattice. Henkelman *et al.*[37] reported that a concerted Li-ion diffusion mechanism around the anti-site defect in $FePO_4$ is found to have a low barrier of 0.35 eV, allowing for facile cross-channel diffusion at room temperature. Using HRTEM, as shown in Fig. 4f, we have observed possible point defects in the fine microstructure of the MBCNW-LFP-HEQD-2 sample, involving combinations of Li vacancies and interstitials, Li^+ on Fe^{2+} sites, Fe^{2+} on Li^+ sites, Fe^{3+} on Fe^{2+} sites, oxygen and Fe^{2+} vacancies.[38] The most of HEQDs embedded in the $LiFePO_4$ nanosheet seem the nearest neighbor antisite defects and α-Li-poor phases ($Li_\alpha FePO_4$) (Fig. 2a) and they have the lowest formation energy of about 0.515–0.550 eV.[39]

Besides, we characterized the elemental distribution mappings of the MBCNW-LFP-HEQD-2 sample at the nanometer level using scanning transmission electron microscopy (STEM) and X-ray energy-dispersive spectrometry (EDS) (Fig. 5). Fig. 5a shows a bright field STEM image of the MBCNW-LFP-HEQD-2 sample. High resolution STEM-EDS analyses show the distributions of Fe, P, O and C of the MBCNW-LFP-HEQD-2 sample in the nanoscale range, respectively (Fig. 5b–e), where

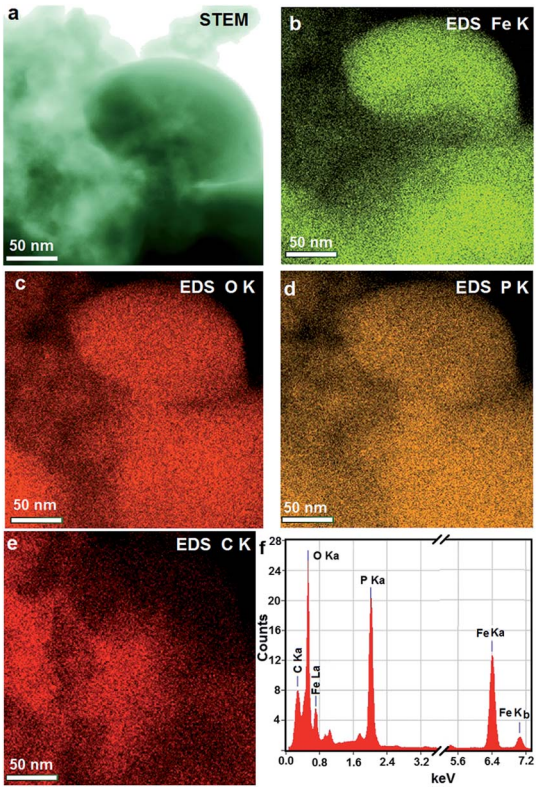

Fig. 5 STEM-EDS images of the MBCNW-LFP-HEQD-2 sample. Bright field STEM image (a) and high resolution STEM-EDS elemental maps of the MBCNW-LFP-HEQD-2 sample. STEM-EDS analysis showing the distributions of Fe, P, O and C of the MBCNW-LFP-HEQD-2 sample in the nanoscale range. Boxed area was scanned for Fe (b), O (c), P (d) and C (e) elemental mapping, respectively. (f) EDS spectra of the MBCNW-LFP-HEQD-2 sample.

Fe, P and O elements are evenly distributed in the nanometer range and C elements are distributed on the surface particles. Fig. 5f shows the EDS spectra of the MBCNW-LFP-HEQD-2 sample, revealing that the sample contains Fe, P, O and C elements, and the atomic ratio of Fe, P, O and C is also close to the stoichiometric proportion of initial reactants. The crystal structure and the mesoporous structure of the different synthetic samples and the ULFPNP sample were evaluated and compared by X-ray diffraction (XRD) and N_2 adsorption–desorption methods (Fig. S2†). The results show that all of samples synthesized under different conditions have an orthorhombic olivine-type structure of pure phase $LiFePO_4$ and the amorphous residual carbon (Fig. S2a†). However, the MBCNW-LFP-HEQD-2 sample possesses better layered structures (Fig. S2b†), better mesoporous structures (Fig. S2c and S3†) and higher crystallinity (Table S3†) through biomineralization processes. It is likely that the high-energy phosphate groups with negative charges in high-energy biomolecule ATP are not only the groups preferentially bonded with iron ions, but also the most important contributor to the free energy barrier for iron phosphate biomineralization at room temperature and pressure.[23] The summary of the structural features and performances for the MBCNW-LFP-HEQDs samples and the ULFPNP sample is given in Tables S2 and S3 in the ESI S3.†

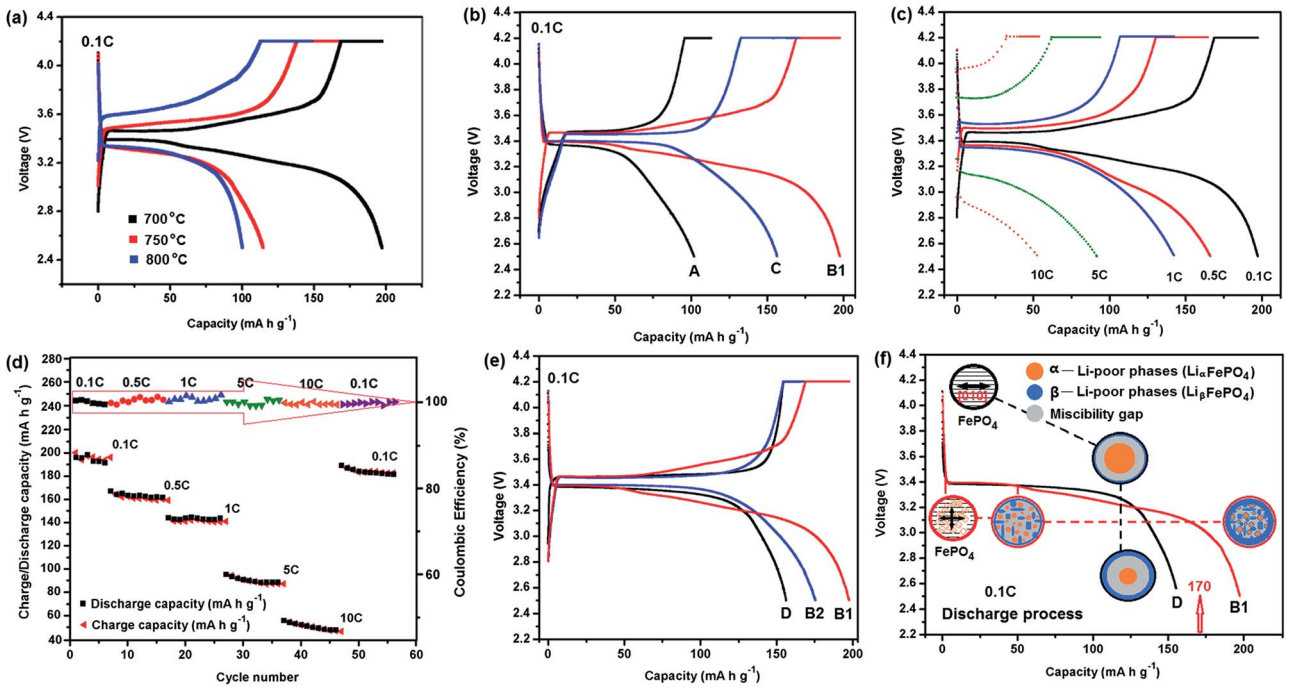

Fig. 6 Electrochemical properties of the different cathodes for the coin cells tested between 2.2 and 4.4. All MBCNW-LFP-HEQD samples have 12.85 wt% C. A is the MBCNW-LFP-HEQD-1 cathode; B1 is the MBCNW-LFP-HEQD-2 cathode; B2 is the MBCNW-LFP-HEQD-2 cathode after 56 cycles at varied current rates: 0.1, 0.5, 1, 5, and 10 C; C is the MBCNW-LFP-HEQD-3 cathode and D is the ULFPNP cathode. (a) First charge–discharge curves of the cathodes synthesized at different temperatures at 0.1 C. (b) First charge–discharge curves of the different cathodes synthesized at 700 °C at 0.1 C. (c) First charge–discharge curves of the MBCNW-LFP-HEQD-2 cathode at different rates. (d) Capacity retention and coulombic efficiency of the MBCNW-LFP-HEQD-2 cathode for 56 cycles at different rates. (e) Comparison of rate capability of the different cathodes. (f) Schematic diagrams of kinetic transformation paths between $LiFePO_4$ and $FePO_4$ in the first discharge process (starting from $FePO_4$) of MBCNW-LFP-HEQD-2 and ULFPNP cathodes at 0.1 C.

The electrochemical performances of the different MBCNW-LFP-HEQD cathodes were evaluated and compared by charge–discharge tests, electrochemical impedance spectroscopy (EIS) and cyclic voltammogram (CV) methods using CR 2032 coin cells. Fig. 6a and b show the first charge–discharge curves of the different cathodes synthesized at different temperatures at 0.1 C, respectively. The MBCNW-LFP-HEQD-2 cathode synthesized at 700 °C delivered a discharge capacity of 197 mA h g^{-1} at a low discharge rate of 0.1 C, which is higher than the theoretical capacity of $LiFePO_4$ (170 mA h g^{-1}). After 56 cycles, the cell still delivered a ultra-high discharge capacity of 180 mA h g^{-1} and retained 91.4% of its initial capacity at the 0.1 C rate (Fig. 6e, B2). To the best of our knowledge, this is the best high discharge capacity performance for the $LiFePO_4$ cathode material reported so far and even better than those of previously reported $LiFePO_4$/C composites.[40–42]

One potential issue of using hybrid materials as electrodes is stability. We tested at different rates and much higher number of cycles for the MBCNW-LFP-HEQD-2 cathode and compared with the existing ULFPNP cathode to more comprehensively evaluate its performance. Although the specific capacity gradually decreases with the increasing current rate (Fig. 6c), a high coulombic efficiency very close to 100% has been achieved at different rates. Even at the high current rate of 10 C, the cell also maintained high coulombic efficiency of 99%. Fig. 6d shows the cyclability of the MBCNW-LFP-HEQD-2 cathode at different rates on which the charge and discharge capacity curves are almost overlapping due to the ultrahigh coulombic efficiency (as shown as the red arrows in the inset). We also compared the rate capability of the MBCNW-LFP-HEQD-2 cathode before and after cycling at different rates. The results are shown in Fig. 6e. The rate capability of the MBCNW-LFP-HEQD-2 cathode after 56 cycles at varied current rates: 0.1, 0.5, 1, 5, and 10 C is 180 mA h g^{-1}. It should be noticed that as long as the current rate reverses back to low current rate, the cell capacity can still be higher than the theoretical capacity of $LiFePO_4$. The original capacity was recovered, confirming structural stability and indicating that the integrity of the MBCNW-LFP-HEQD-2 cathode material has been maintained even after high rate charge and discharge. Fig. S6 in the ESI S2† shows that the MBCNW-LFP-HEQD-2 cathode still retained 91.4% of its initial capacity at the 1 C rate after 100 cycles. These clearly demonstrate that our nanostructure architecture of $LiFePO_4$ with HEQDs is tolerant to varied charge and discharge currents and much higher number of cycles compared with existing electrode materials.

Fig. 6f shows schematic diagrams of kinetic transformation paths between $LiFePO_4$ and $FePO_4$ in the first discharge process of MBCNW-LFP-HEQD-2 (B1) and ULFPNP (D) cathodes at 0.1 C. For the ULFPNP sample, the miscibility gap M_B region is greater than 10 nm (Fig. 2b), resulting in the discharge platform M_B shown in Fig. 2f increases (see the black dotted line path shown in Fig. 6f). In the $LiFePO_4$ nanosheet structure of the

MBCNW-LFP-HEQD-2 sample, it is found that the miscibility gap M_A region was decreased to less than 5 nm by embedding HEQDs (Fig. 2a). This means that solid solution behavior is exhibited in a bigger and more homogenous range in the $LiFePO_4$ structure. So the changed kinetic transformation paths between $LiFePO_4$ and $FePO_4$ in the first discharge process of the MBCNW-LFP-HEQD-2 cathode were changed (see the red dotted line path shown in Fig. 6f), and makes the coexistence of two phases in a single particle unstable. The smaller discharge platform M_A shown in Fig. 2f means that $LiFePO_4$ nanosheets have a short path for lithium intercalation and de-intercalation, also showing the main reason why the specific capacity exceeds the theoretical value at low rate.

The reason why the specific capacity of the synthetic electrode gradually decreases with the increasing current rate could be attributed to many factors. The change of the nanostructure and the decrease of its active surface area for the positive electrode during cycling as well as the increased electrode resistance are suggested to be partly responsibly for reducing the electrochemical reaction rate and capacity. Besides the cathode material itself, other possible factors could be influential, *e.g.*, degradation of the lithium metal foil anode, growth of the passivated surface film layer on the electrodes, decomposition of the binder and the electrolyte, and corrosion of both the current collector and the separator. All these factors will affect the charge transfer kinetics.[43] To better characterize the capacity fading mechanisms with increasing current rate, the electrochemical impedance spectroscopy (EIS) and cyclic voltammogram (CV) performances of the synthetic electrodes are measured as shown in Fig. S4 and S5,† respectively. The diffusion coefficient value D_{Li} of lithium ions is calculated in Table S2c,† which can help to clarify the ohmic resistance and polarization resistance behaviors coincident with capacity loss. The results of EIS and CV tests indicate that the MBCNW-LFP-HEQD-2 electrode has the lower charge transfer resistance and the outstanding reversibility of the lithium extraction/insertion reactions. The electrochemical kinetics of the MBCNW-LFP-HEQD-2 electrode is easier regarding Li^+ extraction than that of the ULFPNP blank electrode and has the better rate performance (please see ESI, Fig. S6†). This is attributed to the excellent nanocomposite of HEQDs embedded inside the crystal structure and mesoporous biocarbon nanowire network coating *in situ* on the surface of $LiFePO_4$ nanosheets.

4. Conclusions

In summary, we have developed the $LiFePO_4$/C nanocomposite by using a multifunctional high-energy biomolecule—ATP, in which HEQDs are embedded in ultra-thin $LiFePO_4$ nanosheet particles and mesoporous biocarbon nanowire interconnected networks were coated on the surface of the nanosheet. By studying the synthesis mechanism we demonstrate that the ATP biomolecules as multifunctional biotemplates are able to control the formation of ultra-thin $LiFePO_4$ nanosheet particles and to direct the HEQDs to be embedded inside the nanosheet structure, and to introduce high-energy phosphate bonds into the crystal structure of $LiFePO_4$ nanoparticles simultaneously. The mesoporous nanoarchitecture ensures not only intimate contact between the liquid electrolyte and active $LiFePO_4$ nanoparticles, but also high electronic conductivity for both facile mass transfer and facile charge transfer. At the low current rate, MBCNW-LFP-HEQD cathodes deliver a much higher specific capacity than the theoretical value and a ultra-high coulombic efficiency. This nanocomposite structure provides high electronic conductivity for enhancing the rate capability of lithium insertion reaction, and scaling up can be readily achieved. Through biomimetic material design, the $LiFePO_4$ cathode material can display electrochemical performances and behaviors for nanoelectronics functionalities.

Although MBCNW-LFP-HEQD nanocomposites have been successfully synthesized and the contributions of HEQDs and mesoporous biocarbon nanowire network structures to $LiFePO_4$ in improving the electrochemical performance have been discussed, some fundamental questions still remain and need to be investigated in detail. An in-depth study of the surface chemistry of MBCNW-LFP-HEQD nanocomposites will direct the optimization of the nature of the nanocomposites. A high tap density of MBCNW-LFP-HEQD nanocomposites is considered to be an important factor for practical applications. An effective route to improve the material's tap density is to design novel structures, including spherical, aggregated and especially microspherical structures composed of tightly compacted nanocrystallites.[5] We have synthesized the cage-like $LiFePO_4$ shell@biocarbon core microspheres with higher discharge energy density at higher current rates by using the same approach combined with hydrothermal treatments. This novel method might become a very competitive candidate for future high energy density C/$LiFePO_4$ production.

Acknowledgements

The authors thank Natural Science Foundation of China (Grant no. 51172132, 51272144, 51042003, 50925205 and 51372142) for the financial support; they also thank the Taishan scholarship program in the field of Glass and Ceramics for the technological support.

Notes and references

1 A. Manthiram, A. Vadivel Murugan, A. Sarkar and T. Muraliganth, *Energy Environ. Sci.*, 2008, **1**, 621.
2 K. T. Lee and J. Cho, *Nano Today*, 2011, **6**, 28.
3 Y. G. Wang, P. He and H. S. Zhou, *Energy Environ. Sci.*, 2011, **4**, 805.
4 K. T. Lee, W. H. Kan and L. F. Nazar, *J. Am. Chem. Soc.*, 2009, **131**, 6044.
5 J. Wang and X. Sun, *Energy Environ. Sci.*, 2012, **5**, 5163.
6 L. X. Yuan, Z. H. Wang, W. X. Zhang, X. L. Hu, J. T. Chen, Y. H. Huang and J. B. Goodenough, *Energy Environ. Sci.*, 2011, **4**, 269.
7 S. Y. Chung, J. T. Bloking and Y. M. Chiang, *Nat. Mater.*, 2002, **1**, 123.
8 Y. J. Lee, H. Yi, W. J. Kim, K. Kang, D. S. Yun, M. S. Strano, G. Ceder and A. M. Belcher, *Science*, 2009, **324**, 1051.

9 C. Delacourt, P. Poizot, J. M. Tarascon and C. Masquelier, *Nat. Mater.*, 2005, **4**, 254.
10 L. H. Hu, F. Y. Wu, C. T. Lin, A. N. Khlobystov and L. J. Li, *Nat. Commun.*, 2013, **4**, 1687.
11 P. G. Bruce, B. Scrosati and J. M. Tarascon, *Angew. Chem., Int. Ed.*, 2008, **47**, 2930.
12 A. Yamada, H. Koizumi, S. I. Nishimura, N. Sonoyama, R. Kanno, M. Yonemura and Y. Kobayashi, *Nat. Mater.*, 2006, **5**, 357.
13 B. Kang and G. Ceder, *Nature*, 2009, **458**, 190.
14 S. I. Nishimura, G. Kobayashi, K. Ohoyama, R. Kanno, M. Yashima and A. Yamada, *Nat. Mater.*, 2008, **7**, 707.
15 R. Malik, F. Zhou and G. Ceder, *Nat. Mater.*, 2011, **10**, 587.
16 K. S. Novoselov, A. K. Geim, S. V. Morozov, D. Jiang, M. I. Katsnelson, I. V. Grigorieva, S. V. Dubonos and A. A. Firsov, *Nature*, 2005, **438**, 197.
17 F. Zhou, T. Maxisch and G. Ceder, *Phys. Rev. Lett.*, 2006, **97**, 155704.
18 Y. B. Zhang, Y. W. Tan, H. L. Stormer and P. Kim, *Nature*, 2005, **438**, 201.
19 O. E. Semonin, J. M. Luther, S. Choi, H. Y. Chen, J. B. Gao, A. J. Nozik and M. C. Beard, *Science*, 2011, **334**, 1530.
20 U. O. S. Seker, T. Ozel and H. V. Demir, *Nano Lett.*, 2011, **11**, 1530.
21 X. G. Zhang, X. D. Zhang, W. He, Y. Z. Yue, H. Liu and J. Y. Ma, *Chem. Commun.*, 2012, **48**, 10093.
22 X. D. Zhang, W. He, Y. Z. Yue, R. M. Wang, J. X. Shen, S. J. Liu, J. Y. Ma, M. Li and F. X. Xu, *J. Mater. Chem.*, 2012, **22**, 19948.
23 X. Y. Du, W. He, X. D. Zhang, Y. Z. Yue, H. Liu, X. G. Zhang, D. D. Min, X. X. Ge and Y. Du, *J. Mater. Chem.*, 2012, **22**, 5960.
24 M. Jensen, R. Keding, T. Hoche and Y. Z. Yue, *J. Am. Chem. Soc.*, 2009, **131**, 2717.
25 F. Borel, R. Q. Han, A. Visser, H. Petry, S. J. H. van Deventer, P. L. M. Jansen and P. Konstantinova, *Hepatology*, 2012, **55**, 821.
26 S. J. Ferguson, *Proc. Natl. Acad. Sci. U. S. A.*, 2010, **107**, 16755.
27 E. Abe, *Chem. Soc. Rev.*, 2012, **41**, 6787.
28 D. B. Williams and C. B. Carter, *Transmission Electron Microscopy: A Textbook For Materials Science*, Springer, New York, NY, USA, 1996.
29 G. Kobayashi, S. I. Nishimura, M. S. Park, R. Kanno, M. Yashima, T. Ida and A. Yamada, *Adv. Funct. Mater.*, 2009, **19**, 395.
30 B. Ellis, L. K. Perry, D. H. Ryan and L. F. Nazar, *J. Am. Chem. Soc.*, 2006, **128**, 11416.
31 P. Gibot, M. Casas-Cabanas, L. Laffont, S. Levasseur, P. Carlach, S. Hamelet, J. M. Tarascon and C. Masquelier, *Nat. Mater.*, 2008, **7**, 741.
32 R. Malik, D. Burch, M. Bazant and G. Ceder, *Nano Lett.*, 2010, **10**, 4123.
33 J. Maier, *Nature*, 2005, **4**, 805.
34 Q. J. Xiang, J. G. Yu and M. Jaroniec, *J. Am. Chem. Soc.*, 2012, **134**, 6575.
35 J. Maier, *Nat. Mater.*, 2005, **4**, 805.
36 Z. S. Wu, L. L. Xue, W. C. Ren, F. Li, L. Wen and H. M. Cheng, *Adv. Funct. Mater.*, 2012, **22**, 3290.
37 G. K. P. Dathar, D. Sheppard, K. J. Stevenson and G. Henkelman, *Chem. Mater.*, 2011, **23**, 4032.
38 G. R. Gardiner and M. S. Islam, *Chem. Mater.*, 2010, **22**, 1242.
39 C. A. J. Fisher, V. M. H. Prieto and M. S. Islam, *Chem. Mater.*, 2008, **20**, 5907.
40 G. X. Wang, H. Liu, J. Liu, S. Z. Qiao, G. Q. Max Lu, P. Munroe and H. Ahn, *Adv. Mater.*, 2010, **22**, 4944.
41 C. M. Doherty, R. A. Caruso, B. M. Smarsly, P. Adelhelm and C. J. Drummond, *Chem. Mater.*, 2009, **21**, 5300.
42 X. L. Wu, L. Y. Jiang, F. F. Cao, Y. G. Guo and L. J. Wan, *Adv. Mater.*, 2009, **21**, 2710.
43 M. K. Mahapatra and R. J. Bodnar, *Appl. Phys. A: Mater. Sci. Process.*, 2009, **95**, 493.

